



TOI-5678b: A 48-day transiting Neptune-mass planet characterized with CHEOPS and HARPS









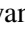

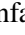

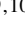



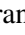

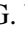


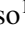



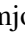




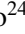
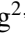
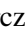
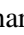
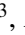


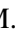
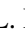









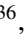

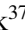













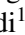
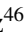




Downloaded from: <https://research.chalmers.se>, 2025-12-04 23:24 UTC

Citation for the original published paper (version of record):

Ulmer-Moll, S., Osborn, H., Tuson, A. et al (2023). TOI-5678b: A 48-day transiting Neptune-mass planet characterized with CHEOPS and HARPS. *Astronomy and Astrophysics*, 674.
<http://dx.doi.org/10.1051/0004-6361/202245478>

N.B. When citing this work, cite the original published paper.

TOI-5678 b: A 48-day transiting Neptune-mass planet characterized with CHEOPS and HARPS★,★★

S. Ulmer-Moll^{1,2} , H. P. Osborn^{2,3} , A. Tuson⁴ , J. A. Egger² , M. Lendl¹ , P. Maxted⁵ , A. Bekkelien¹,
 A. E. Simon² , G. Olofsson⁶ , V. Adibekyan⁷ , Y. Alibert² , A. Bonfanti⁸ , F. Bouchy¹, A. Brandeker⁶ ,
 M. Fridlund^{9,10} , D. Gandolfi¹¹ , C. Mordasini², C. M. Persson¹⁰ , S. Salmon¹ , L. M. Serrano¹¹ ,
 S. G. Sousa⁷ , T. G. Wilson¹² , M. Rieder², J. Hasiba⁸, J. Asquier¹³, D. Sicilia¹⁴ , I. Walter¹⁵ , R. Alonso^{16,17} ,
 G. Anglada^{18,19} , D. Barrado y Navascués²⁰ , S. C. C. Barros^{7,21} , W. Baumjohann⁸ , M. Beck¹ , T. Beck²,
 W. Benz^{2,22} , N. Billot¹ , X. Bonfils²³ , L. Borsato²⁴ , C. Broeg^{2,22} , T. Bárczy²⁵ , J. Cabrera²⁶,
 S. Charnoz²⁷ , M. Cointepas^{1,23}, A. Collier Cameron¹² , Sz. Csizmadia²⁶ , P. E. Cubillos^{28,8}, M. B. Davies²⁹ ,
 M. Deleuil³⁰ , A. Deline¹, L. Delrez^{31,32} , O. D. S. Demangeon^{7,21} , B.-O. Demory²² , X. Dumusque¹,
 D. Ehrenreich^{1,33} , N. L. Eisner³⁴, A. Erikson²⁶, A. Fortier^{2,22} , L. Fossati⁸ , M. Gillon³¹ , N. Grieves¹ ,
 M. Güdel³⁵, J. Hagelberg¹ , R. Helled³⁶, S. Hoyer³⁰ , K. G. Isaak³⁷ , L. L. Kiss^{38,39}, J. Laskar⁴⁰ ,
 A. Lecavelier des Etangs⁴¹ , C. Lovis¹ , D. Magrin²⁴ , V. Nascimbeni²⁴ , J. Otegi¹, R. Ottensammer⁴²,
 I. Pagano¹⁴ , E. Pallé¹⁶ , G. Peter⁴³ , G. Piotto^{24,44} , D. Pollacco⁴⁵, A. Psaridi¹, D. Queloz^{46,47} ,
 R. Ragazzoni^{24,44} , N. Rando¹³, H. Rauer^{26,48} , I. Ribas^{18,19} , N. C. Santos^{7,21} , G. Scandariato¹⁴ ,
 A. M. S. Smith²⁶ , M. Steller⁸ , G. M. Szabó^{49,50}, D. Ségransan¹ , N. Thomas², S. Udry¹ , V. Van Grootel³² ,
 J. Venturini¹, and N. A. Walton⁵¹ 

(Affiliations can be found after the references)

Received 16 November 2022 / Accepted 10 April 2023

ABSTRACT

Context. A large sample of long-period giant planets has been discovered thanks to long-term radial velocity surveys, but only a few dozen of these planets have a precise radius measurement. Transiting gas giants are crucial targets for the study of atmospheric composition across a wide range of equilibrium temperatures and, more importantly, for shedding light on the formation and evolution of planetary systems. Indeed, compared to hot Jupiters, the atmospheric properties and orbital parameters of cooler gas giants are unaltered by intense stellar irradiation and tidal effects.

Aims. We aim to identify long-period planets in the Transiting Exoplanet Survey Satellite (TESS) data as single or duo-transit events. Our goal is to solve the orbital periods of TESS duo-transit candidates with the use of additional space-based photometric observations and to collect follow-up spectroscopic observations in order to confirm the planetary nature and measure the mass of the candidates.

Methods. We use the CHaracterising ExOPlanet Satellite (CHEOPS) to observe the highest-probability period aliases in order to discard or confirm a transit event at a given period. Once a period is confirmed, we jointly model the TESS and CHEOPS light curves along with the radial velocity datasets to measure the orbital parameters of the system and obtain precise mass and radius measurements.

Results. We report the discovery of a long-period transiting Neptune-mass planet orbiting the G7-type star TOI-5678. Our spectroscopic analysis shows that TOI-5678 is a star with a solar metallicity. The TESS light curve of TOI-5678 presents two transit events separated by almost two years. In addition, CHEOPS observed the target as part of its Guaranteed Time Observation program. After four non-detections corresponding to possible periods, CHEOPS detected a transit event matching a unique period alias. Follow-up radial velocity observations were carried out with the ground-based high-resolution spectrographs CORALIE and HARPS. Joint modeling reveals that TOI-5678 hosts a 47.73 day period planet, and we measure an orbital eccentricity consistent with zero at 2σ . The planet TOI-5678 b has a mass of 20 ± 4 Earth masses (M_{\oplus}) and a radius of $4.91 \pm 0.08 R_{\oplus}$. Using interior structure modeling, we find that TOI-5678 b is composed of a low-mass core surrounded by a large H/He layer with a mass of $3.2^{+1.7}_{-1.3} M_{\oplus}$.

Conclusions. TOI-5678 b is part of a growing sample of well-characterized transiting gas giants receiving moderate amounts of stellar insolation ($11 S_{\oplus}$). Precise density measurement gives us insight into their interior composition, and the objects orbiting bright stars are suitable targets to study the atmospheric composition of cooler gas giants.

Key words. planets and satellites: detection – planets and satellites: individual: TOI-5678 – planets and satellites: gaseous planets – methods: data analysis

* Full Table 2 and reduced CHEOPS and HARPS data are only available at the CDS via anonymous ftp to cdsarc.cds.unistra.fr (130.79.128.5) or via <https://cdsarc.cds.unistra.fr/viz-bin/cat/J/A+A/674/A43>

** Based on data from CHEOPS Prog ID: CH_PR110048 and HARPS Prog ID: 108.22L8.001.

1. Introduction

Transiting long-period planets are valuable objects, but they are also challenging to characterize. These planets have a low transit probability, and giant planets have a lower occurrence rate than lower-mass planets (e.g., [Mayor et al. 2011](#); [Petigura et al. 2018](#); [Fulton et al. 2021](#)), which explains why so few of them have been detected so far. Besides, searching for the transit of long-period planets known from radial velocity surveys would be very time consuming, due to the low probability of transit. The four-year baseline of the *Kepler* mission ([Borucki et al. 2010](#)) enabled the characterization of several transiting planets with orbital periods ranging from 100 to 300 days (e.g., [Mancini et al. 2016](#); [Dubber et al. 2019](#); [Dalba et al. 2021](#)), and dedicated searches revealed a few dozen transiting planet candidates with orbital periods between 100 days to several years ([Wang et al. 2015](#); [Uehara et al. 2016](#); [Foreman-Mackey et al. 2016](#)).

The Transiting Exoplanet Survey Satellite (TESS; [Ricker et al. 2015](#)) scans the whole sky, with each TESS sector being observed for 27 days almost continuously. As several subsequent sectors may overlap, some parts of the sky are monitored for up to one year with few interruptions. Exoplanets with orbital periods longer than 27 days will only show one transit event in a TESS sector. Targeting single transit events opens the door to the discovery of planets with longer orbital periods than the ones found by searching periodic events. Several pipelines have thus been developed to search for single transit events (e.g., [Gill et al. 2020a](#); [Montalto et al. 2020](#)). However, the period of these single-transiting candidates is mainly unconstrained. The nature of the TESS survey leads to multiple observations of the same sectors but about two years apart, and consequently the second transit of the same candidate may be detected. The range of possible orbital periods for a duo-transit candidate then becomes reduced to a discrete set of periods. [Osborn \(2022\)](#) have presented a new code to estimate the probability of each period alias. Their classification allows one to prioritize the follow-up of a duo-transit candidate by scheduling observations of the highest-probable periods first. Despite a strong detection bias against planets at long orbital periods, the TESS mission and the efficient follow-up effort has led to an increase of well-characterized transiting long-period giants (e.g., [Gill et al. 2020b](#); [Hobson et al. 2021](#); [Dalba et al. 2022](#); [Ulmer-Moll et al. 2022](#)).

The CHaracterising ExOPlanet Satellite (CHEOPS; [Benz et al. 2021](#)) is the first European Space Agency mission dedicated to the characterization of known exoplanets around bright stars. With space-grade photometric precision, CHEOPS can be used to confirm small transiting planets at long periods (e.g., [Bonfanti et al. 2021](#); [Lacedelli et al. 2022](#)). For the multiplanetary system ν^2 Lupi, the high signal-to-noise ratio of the CHEOPS observations allowed for precise measurement of the radius of its three small planets, as shown by [Delrez et al. \(2021\)](#). Notably, CHEOPS has also been used to recover the orbital periods of TESS duo-transit candidates through targeted observations of the possible period aliases (e.g., [Garai et al. 2023](#); [Osborn et al. 2023](#); [Tuson et al. 2023](#)).

Long-period planets are ideal objects of study to gain insight into the formation and evolution of planetary systems, as their properties are less affected by stellar irradiation and stellar tidal interactions than close-in objects. For transiting planets, their planetary radius is measured with transit photometry, and their planetary mass and eccentricity are often measured through radial velocity follow-up or transit-timing variations, in the case of compact multiplanet systems. These fundamental parameters

govern the planetary mean density and can lead to hints regarding a planet's interior structure.

The study of modestly irradiated giants by [Miller & Fortney \(2011\)](#) and [Thorngren et al. \(2016\)](#) led to the definition of a planetary mass-metallicity relation, putting the metal enhancement of the Solar System giants Jupiter and Saturn in an exoplanetary context. Increasing the sample of long-period transiting exoplanets is essential to refining this relationship and, more broadly, understanding their formation and evolution processes.

This paper reports the discovery and characterization of a long-period Neptune-mass planet transiting TOI-5678. The photometric and spectroscopic observations are described in Sect. 2, along with the observation strategy. Section 3 details the determination of the stellar parameters and the system modeling. The results of the joint modeling and the interior structure model are presented in Sect. 4 and the conclusions in Sect. 5.

2. Observations

The discovery photometry was obtained from the TESS mission (Sect. 2.1), and follow-up photometric observations were performed with the CHEOPS satellite (Sect. 2.2). Ground-based spectroscopic observations were carried out with the high-resolution spectrographs CORALIE (Sect. 2.3) and High Accuracy Radial velocity Planet Searcher (HARPS; Sect. 2.4).

2.1. TESS photometry

The TESS satellite ([Ricker et al. 2015](#)) observed TOI-5678 during its primary and its first extended mission (year 1 and year 3). Until September 2023 (TESS cycle 5), no further TESS observations are planned. TOI-5678 was observed at a two-minute cadence in three TESS sectors: sector 4 (2018-10-18 to 2018-11-15), sector 30 (from 2020-09-22 to 2020-10-21), and sector 31 (2020-10-21 to 2020-11-19).

We discovered a planet candidate in the TESS data using our specialized duo-transit pipeline ([Tuson & the CHEOPS Consortium 2022](#)). This pipeline was created to search for TESS duo-transits suitable for CHEOPS follow-up. The pipeline concatenates the TESS Pre-search Data Conditioned Simple Aperture Photometry (PDCSAP) light curves from the primary and extended mission, detrends the light curve using a mean sliding window, and then runs a box least squares (BLS; [Kovács et al. 2002](#)) transit search on the detrended light curve, with parameters optimized for duo-transit detection. TOI-5678 returned a duo-transit candidate with the first transit at the very beginning of the second orbit of sector 4 and a second transit in sector 30. We checked both transits for asteroid crossing and centroid shifts (indicating a background eclipsing binary) before deciding to pursue follow-up observations. This duo-transit candidate was also independently discovered by the Planet Hunter TESS team and was announced as a Community TESS Object of Interest in March 2021.

The light curves from the primary and extended mission were obtained through the Mikulski Archive for Space Telescopes¹ and the data reduction was done at the Science Processing Operation Center ([Jenkins et al. 2016](#)). We used the PDCSAP fluxes and their corresponding errors for our analysis. We generated target pixel files with *tpfplotter* ([Aller et al. 2020](#)) and used them to check for the presence of contaminant sources, down to a magnitude difference of seven. The apertures that were used to extract the light curves in all three of the sectors are not

¹ mast.stsci.edu

Table 1. CHEOPS photometric observations of TOI-5678.

Visit	Start time [UT]	End time [UT]	Duration [h]	Texp [s]	Alias [days]	File reference
1	2021-09-24 00:54:22	2021-09-24 05:10:29	4.27	60	34.1	CH_PR110048_TG006901_V0200
2	2021-10-10 22:27:20	2021-10-11 02:40:27	4.22	60	39.8 & 59.7	CH_PR110048_TG007201_V0200
3	2021-10-11 03:09:20	2021-10-11 07:36:28	4.45	60	39.8 & 59.7	CH_PR110048_TG007801_V0200
4	2021-10-26 17:44:21	2021-10-26 23:24:30	5.67	60	31.1	CH_PR110048_TG006701_V0200
5	2021-11-03 17:56:20	2021-11-03 23:34:30	5.64	60	47.73	CH_PR110048_TG007501_V0200

Notes. The Alias column corresponds to the period aliases compatible with an expected transit at the date of observation. Texp is the exposure time.

contaminated by neighboring stars. We did not include a dilution factor while modeling the TESS light curves because of the absence of contaminating sources.

2.2. CHEOPS photometry

As a space-based observatory, CHEOPS (Benz et al. 2021) is designed to perform ultra-high precision photometry on bright targets, one star at a time. Science observations with the satellite started in April 2020 and are mainly dedicated to the follow-up of known transiting exoplanets (e.g., Lendl et al. 2020; Bonfanti et al. 2021; Szabó et al. 2021; Barros et al. 2022). The CHEOPS telescope has a 30 cm effective aperture with a 1024 x 1024-pixel, back illuminated Charge-Coupled Device detector (Deline et al. 2020). The CHEOPS bandpass covers a broad range of optical wavelengths, from 330 to 1100 nm. As shown by Lendl et al. (2020), CHEOPS is able to reach a photometric precision of ten parts per million (ppm) per one hour of binning for a very bright star ($V_{\text{mag}} = 6.6$). For faint stars, CHEOPS also complies with its requirement, as it provided a photometric precision of 75 ppm in three hours of integration time for a star of $V_{\text{mag}} 11.9$ (Benz et al. 2021).

TOI-5678 was observed with CHEOPS from 2021-09-24 to 2021-11-03 through the Duos program (CH_PR110048: “Duos, Recovering long period duo-transiting planets”), which is part of the CHEOPS Guaranteed Time Observation program. This program aims to solve the orbital periods of TESS duo-transit candidates around stars with a V magnitude greater than 12. A detailed explanation of the Duos program and its scheduling strategy is presented in Sect. 3.2 of Osborn et al. (2022). The filler program targets candidates with a transit depth between two and four parts per thousand (ppt) such that the observation of a partial transit is sufficient to obtain a detection of the signal. Each CHEOPS visit lasts at least three CHEOPS orbits in order to correctly model instrumental trends and to identify the partial transit. Five CHEOPS visits of TOI-5678 were observed with an exposure time of 60 s. The details of the observations are presented in Table 1. The fifth visit of TOI-5678 showed an ingress, and this transit event uniquely validated the orbital period of the candidate. The CHEOPS light curve is shown in Fig. 1, and no strong systematic trends are visible in the raw data. After this visit, we stopped the monitoring of the target.

TOI-5678 has a V magnitude of 11.4 and is one of the faintest targets to be observed with CHEOPS. We used point spread function (PSF) photometry implemented in the PSF imagerie photometric extraction package (PIPE²) to reduce the CHEOPS data. In the case of TOI-5678, the PIPE data reduction was shown to perform better than the standard the data reduction

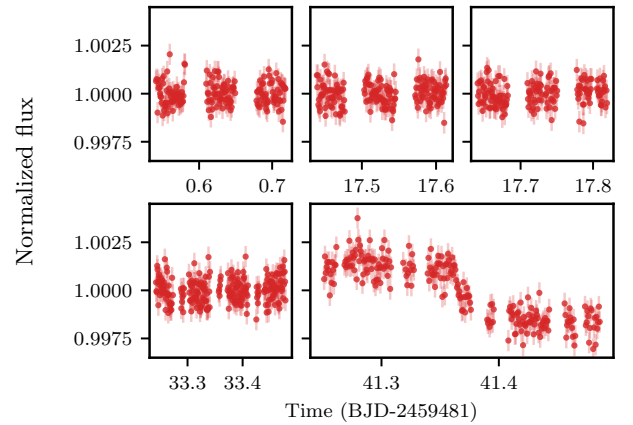


Fig. 1. Raw CHEOPS light curve of TOI-5678 b. The data covers five period aliases and displays an ingress in the bottom-right plot.

pipeline version 13.1 (DRP 13.1; Hoyer et al. 2020). Over the five CHEOPS visits, the average mean absolute deviation of the PIPE light curve is 120 ppm lower than the DRP 13.1 one using the default 25-pixel aperture. We chose to use the PIPE data reduction routines for our analysis. We selected data points without any recognized issue (flag equals zero). We removed data points for which the corresponding background flux has a value higher than $300 \text{ e}^-/\text{pixel}$. The background subtraction routine became unreliable due non-linear behavior beyond this threshold. Along with the time, flux, and errors on the flux, we extracted the background, roll angle (θ), and the X and Y coordinates to be used as detrending vectors in the analysis. We included detrending parameters, which improved the log-evidence values of the fit by a factor of five. The modulation in roll angle is correlated with the estimated contamination by nearby stars, but this contamination is quite low with a mean flux of 0.01% compared to the target mean flux. We found that a linear combination of $\cos(2\theta)$ and $\cos(3\theta)$ was efficient at removing the roll angle dependence. A table of the PIPE reduced CHEOPS photometric observations is available in a machine-readable format at the CDS.

2.3. CORALIE spectroscopy

Spectroscopic vetting and radial velocity follow-up was carried out with CORALIE (Queloz et al. 2001). The high-resolution fiber-fed spectrograph CORALIE is installed at the Nasmyth focus of the Swiss 1.2 m *Euler* telescope (La Silla, Chile)³. CORALIE has a spectral resolution of 60 000, and the sampling per resolution element is equal to three pixels. Two fibers

² github.com/alphapsa/PIPE

³ eso.org/public/teles-instr/lasilla/swiss

Table 2. Radial velocities of TOI-5678.

Time BJD	RV [ms ⁻¹]	RV error [ms ⁻¹]	Instrument
2 459 464.78269	-3.86711	25.68928	CORALIE
2 459 470.72244	49.11076	27.98340	CORALIE
2 459 475.74732	36.17593	18.78204	CORALIE
...			
2 459 622.55655	55.81805	2.972752	HARPS
2 459 624.56960	51.25084	2.803944	HARPS
2 459 625.53665	54.48176	2.21336	HARPS

Notes. Full table is available at the CDS.

were used for the fiber injection. The first fiber was dedicated to the target observation, and the second fiber could collect light from a Fabry-Pérot etalon or the sky to allow for simultaneous wavelength calibration or background subtraction.

TOI-5678 was observed with CORALIE as part of a support program for CHEOPS to vet the candidates with spectroscopy and to evaluate the level of stellar activity visible in the radial velocity. Two high-resolution spectra were obtained several days apart. These observations are useful to rule out clear eclipsing binary scenarios. TOI-5678 was then monitored at a low cadence to reveal possible long-term trends or strong activity signals.

We used the standard data reduction pipeline to extract the stellar radial velocities using the cross-correlation technique. The stellar spectrum of TOI-5678 is cross-correlated with a G2 mask, which is the closest mask to the stellar type to obtain a cross-correlation function (CCF; e.g., [Pepe et al. 2002](#)). The outputs of the pipeline are the radial velocity and its associated error as well as additional parameters derived from the CCF, such as the full width half maximum (FWHM), contrast, and bisector inverse slope (BIS).

We collected 14 radial velocity measurements of TOI-5678 (from 2021-09-07 to 2022-01-23) with an exposure time varying between 1800 and 2100 s, depending on the observing conditions. The radial velocity observations are detailed in Table 2.

2.4. HARPS spectroscopy

Once the orbital period of the candidate was solved with CHEOPS observations, we decided to add TOI-5678 to an ongoing HARPS program dedicated to the follow-up of warm transiting giants (108.22L8.001, PI: Ulmer-Moll). A fiber-fed spectrograph, HARPS has a spectral resolution of about 115 000. It is installed at the 3.6 m telescope in La Silla, Chile ([Mayor et al. 2003](#)). TOI-5678 was observed with the high-accuracy mode of HARPS from 2021-11-12 to 2022-02-15, and we obtained 23 HARPS measurements with an exposure time varying between 1800 and 2100 s. The average signal-to-noise ratio is equal to 40 at 550 nm. The radial velocity observations are presented in Table 2. The data reduction was performed with the standard data reduction pipeline ([Lovis & Pepe 2007](#)). The radial velocities were extracted with the cross-correlation technique using a G2 mask. Along with the radial velocities, the CCFs are used to derive several stellar activity indicators, such as the FWHM, contrast, and BIS. Additional parameters were also extracted from the spectra, namely, the S, H α , Na, and Ca indexes. The HARPS spectra were co-added in order to derive stellar parameters, and the analysis is detailed in Sect. 3.1.

3. Methods

3.1. Stellar parameter determination

In order to derive precise stellar parameters, the HARPS spectra of TOI-5678 were doppler-shifted according to their radial velocity measured during the data reduction and co-added in a single 1D master spectrum. We used ARES+MOOG to derive stellar atmospheric parameters (T_{eff} , $\log g$, microturbulence, [Fe/H]) following the same methodology described in [Santos et al. \(2013\)](#); [Sousa \(2014\)](#), and [Sousa et al. \(2021\)](#). The latest version of ARES⁴ ([Sousa et al. 2007, 2015](#)) was used to consistently measure the equivalent widths of selected iron lines based on the line list presented in [Sousa et al. \(2008\)](#). A minimization process was used in this spectral analysis to find ionization and excitation equilibrium and converge to the best set of spectroscopic parameters. The iron abundances were computed using a grid of Kurucz model atmospheres ([Kurucz 1993](#)) and the radiative transfer code MOOG ([Snedden 1973](#)). The converged spectroscopic parameters are listed in Table 3. The stellar abundances [Mg/H] = 0.07 ± 0.06 dex and [Si/H] = 0.00 ± 0.04 dex were derived using the classical curve-of-growth analysis method, assuming local thermodynamic equilibrium (e.g., [Adibekyan et al. 2012, 2015](#)). The same codes and models were used for the abundance determinations.

To determine the stellar radius of TOI-5678, we used a Markov chain Monte Carlo infrared flux method (MCMC IRFM; [Blackwell & Shallis 1977](#); [Schanche et al. 2020](#)) that computes the stellar angular diameter and effective temperature via known relationships of these properties and the apparent bolometric flux. We used the stellar spectral parameters as priors to construct a spectral energy distribution from stellar atmospheric models that were attenuated via extinction estimates and used to compute the bolometric flux that is compared to the observed data taken from the most recent data releases for the bandpasses *Gaia* G, *G_{BP}*, and *G_{RP}*; 2MASS *J*, *H*, and *K*; and WISE W1 and W2 ([Skrutskie et al. 2006](#); [Wright et al. 2010](#); [Gaia Collaboration 2021](#)), with the stellar atmospheric models taken from the ATLAS catalogs ([Castelli & Kurucz 2003](#)). By converting the stellar angular diameter to the stellar radius using the offset corrected *Gaia* Early Data Release 3 parallax ([Lindgren et al. 2021](#)), we obtained $R_{\star} = 0.938 \pm 0.007 R_{\odot}$.

Finally, assuming T_{eff} , [Fe/H], and R_{\star} as input parameters, we determined the isochronal mass M_{\star} and age t_{\star} by using two different stellar evolutionary models. The first pair of mass and age values was computed through the isochrone placement algorithm ([Bonfanti et al. 2015, 2016](#)), which interpolates the input parameters within pre-computed grids of PARSEC⁵ v1.2S ([Marigo et al. 2017](#)) isochrones and tracks. The second pair of mass and age values was retrieved by the Code Liégeois d'Évolution Stellaire (CLES; [Scuflaire et al. 2008](#)) code, which computes the best-fit stellar evolutionary tracks following the Levenberg-Marquadt minimization scheme as presented in [Salmon et al. \(2021\)](#). After carefully checking for the mutual consistency of the two respective pairs of outcomes through the χ^2 -based criterion broadly discussed in [Bonfanti et al. \(2021\)](#), we merged the output distributions of both the stellar mass and age, ending up with the following estimates: $M_{\star} = 0.905^{+0.039}_{-0.041} M_{\odot}$ and $t_{\star} = 8.5 \pm 3.0$ Gyr. The results are presented in Table 3.

⁴ The latest version, ARES v2, can be downloaded at <https://github.com/sousasag/ARES>

⁵ Padova and TRieste Stellar Evolutionary Code: <http://stev.oapd.inaf.it/cgi-bin/cmd>

Table 3. Stellar properties and stellar parameters.

TOI-5678		
Other names		
2MASS	J03093220-3411530	2MASS
<i>Gaia</i>	5048310370810634624	<i>Gaia</i>
TYC	7022-00871-1	<i>Tycho</i>
TESS	TIC 209464063	TESS
TOI	TOI-5678	TESS
Astrometric properties		
RA	03:09:32.2	TESS
Dec	−34:11:54.53	TESS
μ RA [mas yr ^{−1}]	−5.565±0.032	<i>Gaia</i> DR3
μ Dec [mas yr ^{−1}]	−89.15±0.04	<i>Gaia</i> DR3
Parallax [mas]	6.099±0.014	<i>Gaia</i> DR3
Photometric properties		
TESS [mag]	10.669±0.006	TESS
<i>V</i> [mag]	11.438±0.012	<i>Tycho</i>
<i>B</i> [mag]	12.031±0.171	<i>Tycho</i>
<i>G</i> [mag]	11.1483±0.0004	<i>Gaia</i>
<i>J</i> [mag]	9.997±0.022	2MASS
<i>H</i> [mag]	9.699±0.021	2MASS
<i>Ks</i> [mag]	9.563±0.023	2MASS
W1 [mag]	9.533±0.023	WISE
W2 [mag]	9.591±0.02	WISE
W3 [mag]	9.552±0.033	WISE
W4 [mag]	9.433±0.524	WISE
TESS luminosity [<i>L</i> _⊙]	0.740±0.025	TESS
Bulk properties		
<i>T</i> _{eff} [K]	5485 ± 63	Sect. 3.1
Spectral type	G7V	Sect. 3.1
log <i>g</i> [cm s ^{−2}]	4.34 ± 0.11	Sect. 3.1
<i>V</i> _t micro [km s ^{−1}]	0.82 ± 0.03	Sect. 3.1
[Fe/H] [dex]	0.00 ± 0.01	Sect. 3.1
[Mg/H] [dex]	0.07 ± 0.06	Sect. 3.1
[Si/H] [dex]	0.00 ± 0.04	Sect. 3.1
<i>v</i> sin <i>i</i> [km s ^{−1}]	3.1 ± 1.0	Sect. 3.1
Age [Gyr]	8.5 ± 3.0	Sect. 3.1
Radius [<i>R</i> _⊙]	0.938 ± 0.007	Sect. 3.1
Mass [<i>M</i> _⊙]	0.905 ^{+0.039} _{−0.041}	Sect. 3.1

References. 2MASS: [Skrutskie et al. \(2006\)](#); *Gaia* EDR3: [Gaia Collaboration \(2021\)](#); TESS: ([Stassun et al. 2019](#)); *Tycho*: ([Høg et al. 2000](#)); WISE: [Wright et al. \(2010\)](#).

Following procedures going back to the CoRoT mission ([Fridlund 2008](#)), we applied the Interactive Data Language package Spectroscopy Made Easy ([Piskunov et al. 1995](#); [Valenti & Piskunov 1996](#); [Piskunov & Valenti 2017](#)). With this code, and using the stellar parameters given above as fixed inputs, we then synthesized a spectrum based on the well-determined stellar atmospheric grid MARCS 2012 ([Gustafsson et al. 2008](#)) using atomic and molecular parameters from the Vienna Atomic Line Database ([Piskunov et al. 1995](#)) for the synthesis. Again following schemes outlined in [Fridlund et al. \(2020\)](#), and references therein, and while keeping the turbulent velocities *V*_t macro and *V*_t micro fixed at the empirical values found in the literature ([Gray 2008](#); [Bruntt et al. 2010](#); [Doyle et al. 2014](#)), we found *v* sin *i* to be 3.1±1 km s^{−1}.

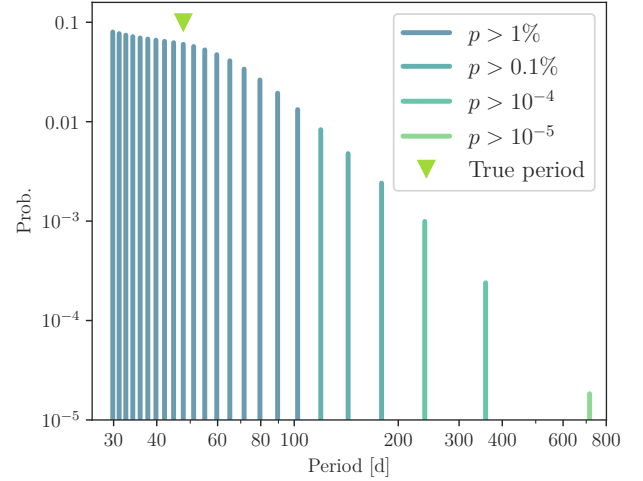


Fig. 2. Marginalized probabilities of the possible period aliases, obtained with MonoTools, from TESS data only. The triangle indicates the true period of TOI-5678 b.

3.2. TESS photometric analysis

We selected TOI-5678 as a potential target for the CHEOPS Duos program, as its TESS light curve presents two single transits separated by a data gap of about 716 days. As for all targets in this CHEOPS program, we ran a photometric analysis with the software package MonoTools ([Osborn 2022](#))⁶. MonoTools is especially adapted to detecting, vetting, and modeling multi-planet systems in the case of single- and duo-transiting planets. The first step was to verify that the transit is not due to a rise in the background flux, which is indicative of an asteroid crossing or an artifact. We also tested that the transit model is a better fit to the event compared to a sine wave or a polynomial function. We checked that there was no feature in the *X* and *Y* coordinates coincident with the transit event, which would indicate a possible eclipsing binary or blend scenario. Finally, we confirmed that the shape, depth, and duration of the two transit events are compatible.

The second step was to model the duo-transit in order to determine which period aliases to observe. MonoTools uses a Bayesian framework to marginalize over the possible period aliases and compute the probability distribution of the period aliases, as shown in Fig. 2. This method fits the impact parameter, transit duration, and radius ratio in a way that is agnostic of the exoplanet period. When combined with stellar parameters, such as bulk density ([Stassun et al. 2019](#)), the transit model allowed us to derive an instantaneous transverse planetary velocity and, therefore, to compute a marginalized probability distribution for each allowed period alias. This method uses a combination of the model likelihood and priors from a combination of window function and occurrence rate (P^{-2} ; [Kipping 2018](#)), a geometric transit probability ($p_g \propto a^{-1} \sim P^{-2/3}$; e.g., [Winn 2010](#)), and an eccentricity prior ([Kipping 2013b](#)). For each allowed period alias, the eccentricity prior was applied using the eccentricity distribution implied by the ratio of the transverse planetary velocity to the circular velocity at that period.

Once the probabilities of the different period aliases were computed, we organized the CHEOPS observations. We scheduled 13 of the highest-probability aliases (covering a sum of 85% of the probability space) on CHEOPS; however, due to scheduling constraints, only a fraction of these are likely to be

⁶ github.com/hposborn/MonoTools

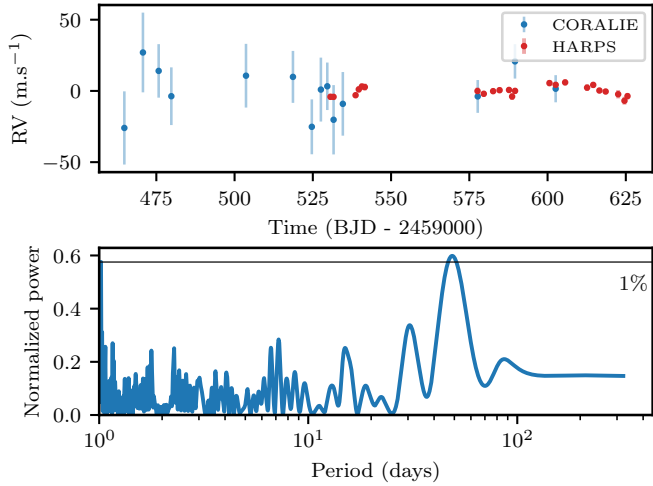


Fig. 3. Top: time series of radial velocities from CORALIE (blue dots) and HARPS (red triangles) for TOI-5678. The HARPS error bars are smaller than the marker. Bottom: generalized Lomb-Scargle periodogram of the radial velocities (blue line). The 1% false alarm probability level is indicated with a black line. The highest peak corresponds to a period of about 48.8 days.

observed. The transits of TOI-5678 b are sufficiently deep such that CHEOPS does not require full transit coverage in order to successfully recover a transit. We chose to only schedule partial transits, which required 2.8-orbit (4.6-h) observations for each alias. We left a large degree of flexibility regarding the start time such that at least one orbit of in-transit data would always be observed. This flexibility improves the likelihood of observations of TOI-5678 b aliases being selected by the CHEOPS scheduler, even at low internal priority.

We realized *a posteriori* that the data from the first observation, labeled “visit 1” in Table 1, covers only in-transit times. At first, this visit was inconclusive since we did not have any baseline signal. Further observations proved that visit 1 is in agreement with the baseline flux and rules out the 34.1-day period alias. Visits 2 and 3 cover the period aliases 39.8 days and 59.7 days, respectively, and we obtained a clear non-detection of the transit signal⁷. Visit 4 covers the 31.1-day period alias and also results in a clear non-detection. Visit 5 covers the 47.73-day alias, and a transit ingress was detected. We stopped the CHEOPS observations after the successful detection in the fifth visit.

3.3. Radial velocity analysis

The CORALIE observations of TOI-5678 show a low radial velocity root mean square of 15 ms^{-1} over two months, for an average radial velocity precision of 20 ms^{-1} . The preliminary analysis of the TESS data and the period recovery work done with CHEOPS result in a planetary candidate with an orbital period of 47.73 days and a radius of $4.9 R_{\oplus}$. From these parameters, we estimated the expected mass of the planetary candidate to be between 18 and $21.5 M_{\oplus}$ (based on the empirical mass-radius relations from [Bashi et al. 2017](#) and [Otegi et al. 2020](#), respectively), leading to an expected semi-amplitude, ranging from 3.3 to 3.8 ms^{-1} . With the HARPS Exposure Time

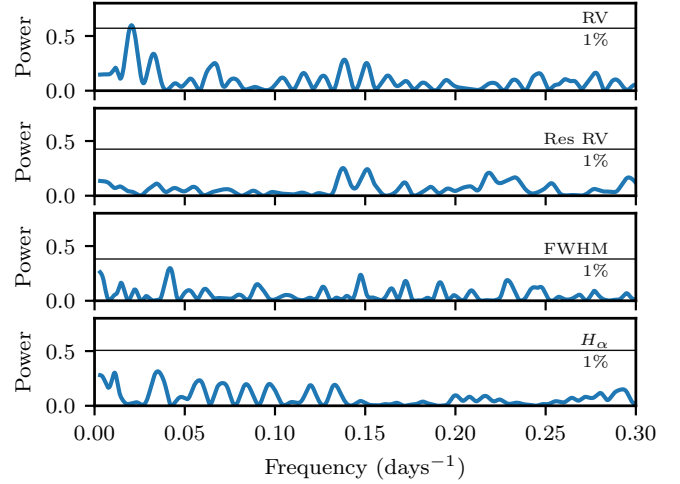


Fig. 4. Generalized Lomb-Scargle periodogram of the radial velocities, radial velocity residuals, FWHM, and H_{α} index (from top to bottom). The 1% false alarm probability level is indicated with a black line.

Calculator⁸, we computed that the expected radial velocity precision achievable with a 1800-s HARPS exposure is 1.4 ms^{-1} for TOI-5678. A detection of the radial velocity signal was feasible during the next few months of observability (November to February). The target was then selected to be added to an ongoing HARPS program with the planned goal of characterizing long-period transiting exoplanets. Figure 3 presents the radial velocity dataset of TOI-5678 and its corresponding generalized Lomb-Scargle (GLS) periodogram ([Zechmeister & Kürster 2009](#)), which combines both CORALIE and HARPS datasets. No significant peak was found in the GLS periodogram of the following stellar activity indicators: FWHM and bisector of the CCF or the H_{α} index. The GLS periodogram of the CCF contrast shows some peaks at periods unrelated to the period of the planetary candidate. Figure 4 displays the GLS periodogram of the CORALIE and HARPS radial velocities, the FWHM of the CCF, and the H_{α} index. The radial velocity residuals were calculated by removing the best-fit Keplerian model from the joint analysis in Sect. 3.4.

A preliminary analysis of the radial velocity dataset was performed with the software package *kima* ([Faria et al. 2018](#)), which is dedicated to the analysis of multiplanetary systems and takes into account the radial velocity time series and their associated activity indicators. Using a Bayesian framework, *kima* models radial velocity data as a sum of Keplerian functions. Data from different spectrographs can be considered with a free radial velocity offset between datasets. The number of planets is a free parameter of the model, and we chose to set it to a prior uniformly distributed as either zero, one, or two. We set the maximum value of the orbital period prior to the time span of the dataset, and the upper bound of the semi-amplitude prior was set to twice the peak-to-peak of the radial velocities. Table A.1 lists all priors used in this analysis.

The analysis of the CORALIE and HARPS data of TOI-5678 with *kima* led to a detection of one planetary signal with an orbital period of $48.63^{+2.61}_{-2.29}$ days and a semi-amplitude of $3.94^{+0.79}_{-0.82} \text{ ms}^{-1}$. The Bayes factor between the no planet and one planet model is equal to 52 and 0.6 between the one planet and two planet model. While the Bayes factor for the one planet model is not superior to 150, a common threshold for significance, it indicates moderate evidence for this model

⁷ One of the two visits would have been enough to exclude both aliases, but the Mission Planning System automatically scheduled both visits and we did not remove one of them.

⁸ eso.org/observing/etc

(Feroz et al. 2011). The presence of transits with a compatible period adds credibility to the signal.

3.4. Joint analysis

We combined the photometric and radial velocity data to perform an analysis of the planetary system around TOI-5678. We used the software package *juliet* (Espinoza et al. 2019) to jointly model the datasets, as *juliet* models multiplanetary systems, including transiting and non-transiting planets, within a Bayesian framework. The light curve modeling in *juliet* is based on *batman* (Kreidberg 2015) for the model of the planetary transits. The stellar activity and instrumental correlations can be specified with Gaussian processes or parametric functions, including linear models (LMs). Photometric datasets from different instruments can be included in the model by adding independent jitter and offset terms as well as dilution factors. To model the Keplerian orbits in the radial velocity data, we used *RadVel* (Fulton et al. 2018). Several sampling methods can be implemented in *juliet*, and we chose the nested sampling method *dynesty* (Speagle 2019). Data from multiple instruments can be incorporated using separate values for radial velocity jitter by allowing for offsets between the datasets.

Two planetary transits are visible in the TESS data in sectors 4 and 30. We chose to include these two relevant sectors and to exclude sector 31, which does not contain any transit feature. Since only the fifth CHEOPS visit displays a partial transit of TOI-5678 b, we chose to only include this last visit for the joint modeling. The model parameters for the planet are the orbital period, the planet-to-star radius ratio, the mid-transit time of the first transit, the impact parameter, the argument of periastron, and the eccentricity. Notably, we used a Beta prior for the eccentricity and a uniform prior between 40 and 60 days for the orbital period. We compared the evidence values of different fits in order to choose the detrending of the TESS data (inclusion of Gaussian processes) and the modeling of the eccentricity. We checked the impact of the eccentricity Beta prior by changing it from a Beta prior to a uniform prior between zero and one. We found that both priors lead to similar posterior distributions as well as an eccentricity of $0.14^{+0.07}_{-0.07}$ for the Beta prior and $0.15^{+0.06}_{-0.08}$ for the uniform prior. Regarding the stellar density, we found that the density derived from the TESS photometric fit with *MonoTools* is in agreement with the one derived in Sect. 3.1. In this joint fit, the stellar density is governed by a normal prior informed by the stellar spectroscopic analysis done in Sect. 3.1. Because the TESS and CHEOPS bandpasses are different, we modeled the limb darkening with a quadratic law using two different sets of q_1 and q_2 parameters (Kipping 2013a). The priors used in the limb-darkening parameters were derived from the LDCU⁹ code, which is a modified version of the python routine implemented by Espinoza & Jordán (2015). It computes the limb-darkening coefficients and their corresponding uncertainties using a set of stellar intensity profiles that account for the uncertainties in the stellar parameters. The stellar intensity profiles were generated based on two libraries of synthetic stellar spectra: ATLAS (Kurucz 1979) and PHOENIX (Husser et al. 2013). Table B.1 details the priors used for all the model parameters.

The TESS photometric variability was taken into account in one Gaussian process for each sector using an approximate Matern kernel. The CHEOPS light curves are known to have trends correlated with the roll angle of the spacecraft. Therefore, we used LMs to decorrelate the CHEOPS data. The following

Table 4. Fitted and derived parameters for TOI-5678 b.

Parameters	TOI-5678 b
Fitted parameters	
Orbital period [days]	$47.73022^{+0.00014}_{-0.00013}$
Time of transit T0 [days]	$2458424.7059^{+0.0035}_{-0.0032}$
Radius ratio	$0.0480^{+0.0007}_{-0.0007}$
Impact parameter	$0.17^{+0.13}_{-0.10}$
Stellar density [kg m^{-3}]	1551^{+83}_{-95}
TESS limb darkening q_1	$0.351^{+0.027}_{-0.028}$
TESS limb darkening q_2	$0.302^{+0.010}_{-0.011}$
CHEOPS limb darkening q_1	$0.46^{+0.04}_{-0.04}$
CHEOPS limb darkening q_2	$0.363^{+0.013}_{-0.013}$
Eccentricity	$0.14^{+0.07}_{-0.07}$
Argument of periastron	208^{+18}_{-11}
Radial velocity semi-amplitude [ms^{-1}]	$3.8^{+0.7}_{-0.7}$
Derived parameters	
Planetary radius [R_{\oplus}]	$4.91^{+0.08}_{-0.08}$
Planetary mass [M_{\oplus}]	20^{+4}_{-4}
Inclination [degrees]	$89.83^{+0.11}_{-0.12}$
Semi major axis [au]	$0.249^{+0.005}_{-0.005}$
Transit duration [hours]	$6.96^{+0.10}_{-0.10}$
Equilibrium temperature [K]	513^{+8}_{-7}
Instrumental parameters	
TESS offset	$-0.00002^{+0.00009}_{-0.00008}$
TESS jitter [ppm]	$1.9^{+13.6}_{-1.6}$
TESS 2 offset	$-0.00002^{+0.00005}_{-0.00005}$
TESS 2 jitter [ppm]	$1.5^{+11.2}_{-1.3}$
CHEOPS offset	$-0.00121^{+0.00008}_{-0.00008}$
CHEOPS jitter [ppm]	123^{+84}_{-91}
GP amplitude TESS (relative flux)	$0.000028^{+0.00009}_{-0.00006}$
GP time-scale TESS [days]	$0.9^{+0.4}_{-0.3}$
GP amplitude TESS 2 (relative flux)	$0.00015^{+0.00007}_{-0.00004}$
GP time-scale TESS 2 [days]	$1.2^{+0.09}_{-0.5}$
Background CHEOPS (relative flux)	$-0.00014^{+0.00006}_{-0.00006}$
$\cos(2\theta)$ CHEOPS [days]	$0.00023^{+0.00011}_{-0.00012}$
$\cos(3\theta)$ CHEOPS [days]	$0.00014^{+0.00008}_{-0.00008}$
X coordinate CHEOPS	$-0.00020^{+0.00005}_{-0.00005}$
Y coordinate CHEOPS	$-0.00016^{+0.00005}_{-0.00005}$
CORALIE offset [ms^{-1}]	24.0^{+4}_{-4}
HARPS offset [ms^{-1}]	$59.7^{+0.5}_{-0.5}$
CORALIE jitter [ms^{-1}]	3.0^{+4}_{-2}
HARPS jitter [ms^{-1}]	$1.3^{+0.4}_{-0.2}$

parameters were scaled and then used for linear decorrelation: background flux, cosine of the roll angle, and the X and Y coordinates. A preliminary analysis of the CHEOPS data allowed us to select the relevant detrending parameters by comparing evidence values of the fits. The functional form of the detrending for the fifth CHEOPS visit is presented in Sect. 2.2 and in Table 4. The priors on the associated coefficients are all uniform between -1 and 1 because the parameters were normalized and scaled. The photometric and instrumental variabilities were fitted simultaneously with the transit model.

⁹ <https://github.com/delinea/LDCU>

The additional parameters included for the radial velocity data are the radial velocity semi-amplitude and jitters and offsets for the two instruments (CORALIE and HARPS). The radial velocity analysis in Sect. 3.3 shows that the HARPS rms is equal to 2 ms^{-1} . This value is comparable to the average uncertainty of the HARPS radial velocity (1.4 ms^{-1}); thus, we did not add parametric functions or Gaussian processes to model additional non-white noise. We ran the final fit using the nested sampling algorithm with 2000 live points and until the uncertainty regarding the log evidence was smaller than 0.1.

4. Results and discussion

4.1. Planetary system around TOI-5678

Our joint analysis shows that TOI-5678 hosts a transiting planet with an orbital period of 47.73 days, a planetary mass of $20 \pm 4 M_{\oplus}$, and a planetary radius of $4.91 \pm 0.08 R_{\oplus}$. The transit has a total duration of $6.96 \pm 0.10 \text{ h}$, and the semi-major axis is $0.249 \pm 0.005 \text{ au}$. The orbital eccentricity is equal to 0.14 ± 0.07 and is consistent at 2σ with a circular orbit. We note that a circular fit is only marginally disfavored when compared to a fit with free eccentricity ($\Delta \ln Z < 2$). We estimated the tidal circularization timescale with two formulas: one from Adams & Laughlin (2006) and the other from Jackson et al. (2008). We chose a tidal quality factor for the planet Q_p of 10^5 , which is within the range of values estimated for the ice and gas giants of the Solar System (Banfield & Murray 1992; Lainey et al. 2009). The stellar tidal quality factor varied between 10^5 and 10^8 (Bonomo et al. 2016), without a significant effect on the timescale. With both formalisms, we found a circularization timescale on the order of 20 000–25 000 Gyr. This timescale is much larger than the age of the system ($8.5 \pm 3.0 \text{ Gyr}$) and suggests that the orbit of TOI-5678 b is not subject to tidal circularization.

The HARPS phase-folded radial velocities are shown in Fig. 5 with the median radial velocity model. TOI-5678 b induces a radial velocity signal with a semi-amplitude of $3.8 \pm 0.7 \text{ ms}^{-1}$. The HARPS jitter is $1.3^{+0.4}_{-0.2} \text{ ms}^{-1}$ and the HARPS rms is about 2.1 ms^{-1} . The CORALIE radial velocities were used for the joint fit; they are not displayed in Fig. 5 due to their large scatter and for improved readability. After five months of radial velocity monitoring, we did not measure any significant drift.

Figure 6 presents the TESS light curves modeled with Gaussian process regression and the CHEOPS light curve modeled with a combination of linear functions. The standard deviation of the two-minute, ten-minute, and one-hour binned residuals for the TESS light curves are 1430, 650, 260 ppm for sector 4 and 1480, 660, 265 ppm for sector 30, respectively. The full model of sector 4 appears flat in the top-left panel of Fig. 6 because the variations of the Gaussian process model are smaller in comparison to the transit depth. The CHEOPS data have a standard deviation of the two-minute, ten-minute, and one-hour binned residuals of 450, 200, 110 ppm. The posterior distributions of the fitted parameters for TOI-5678 b along with the stellar density and radial velocity semi-amplitude are presented in Fig. C.1. Table 4 details the final parameters and associated uncertainties of TOI-5678 b.

4.2. TOI-5678 b within the exoplanet population

TOI-5678 b joins the growing sample of transiting exoplanets with orbital periods larger than 15 days and sizes between Neptune and Saturn (e.g., Dalba et al. 2020; König et al. 2022). At the lower limit in mass of the group of planets between the

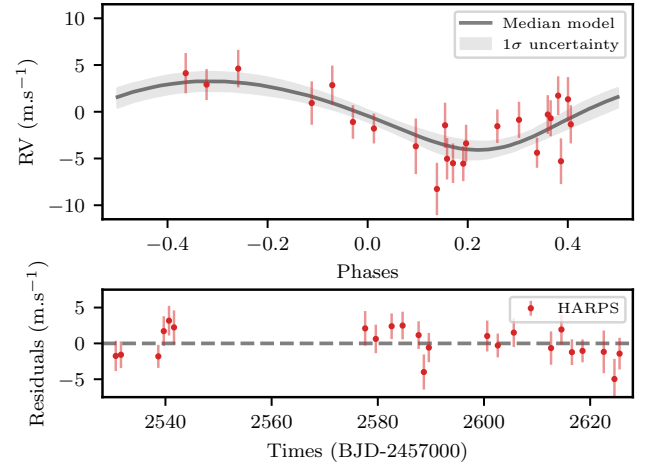


Fig. 5. Radial velocities of TOI-5678. Top: HARPS radial velocities (red dots) as a function of orbital phase. The median Keplerian model (gray line) is plotted along with its corresponding 1σ uncertainty (gray shaded area). Bottom: radial velocity residuals (red dots) as a function of time.

ice and gas giants, TOI-5678 b is an interesting object of study for its formation mechanism. Under the core accretion scenario, the planetary core is formed early enough to accrete gas from the protoplanetary disk, but a relatively small final mass indicates that gas accretion has stopped and prevented the formation of a gas giant. For example, Dransfield et al. (2022) discovered a multiplanetary system of three long-period transiting sub-Neptunes, with orbital periods of 22, 56, and 84 days. The planets have very different mean densities, which displays the different outcomes of planetary formation and evolution within one system. The diversity of intermediate-mass exoplanets seems to be easily explained when studying the formation of Uranus and Neptune (Helled & Bodenheimer 2014; Valletta & Helled 2022). The authors demonstrate that slight changes in the protoplanetary disk and the environment of the planetary embryos (e.g., core accretion rate, solid surface density) lead to planets with greater differences in mass and composition.

We present TOI-5678 b within the population of transiting exoplanets in Fig. 7. We downloaded the NASA exoplanet database¹⁰ on February 28, 2023, and selected confirmed exoplanets with radius uncertainties lower than 8% and mass uncertainties lower than 20%. With a planetary radius of $4.91 \pm 0.08 R_{\oplus}$ and a stellar insolation of $11.5 \pm 0.7 S_{\oplus}$, TOI-5678 b is larger than the planets in the group of volatile-rich sub-Neptunes. The planetary mean density of TOI-5678 b is equal to $0.170 \pm 0.034 \rho_{\oplus}$, suggesting that the planet could host a large fraction of water or gas. When compared to Neptune, TOI-5678 b has a similar mass ($1.17 \pm 0.23 M_{\oplus}$) but a larger radius ($1.262 \pm 0.021 R_{\oplus}$), implying a lower planetary mean density ($0.57 \rho_{\oplus}$). We investigate the interior structure in detail in the following section.

Additional information on the formation and evolution of warm exoplanets can be obtained through study of their atmospheres and their spin-orbit angles. We estimated the transmission spectrum metric (TSM; Kempton et al. 2018) of TOI-5678 b to be 40. This TSM value is rather low but still places TOI-5678 b in the top five targets with radii superior or equal to Neptune receiving less than $25 S_{\oplus}$ (upper-right corner of Fig. 7).

¹⁰ exoplanetarchive.ipac.caltech.edu

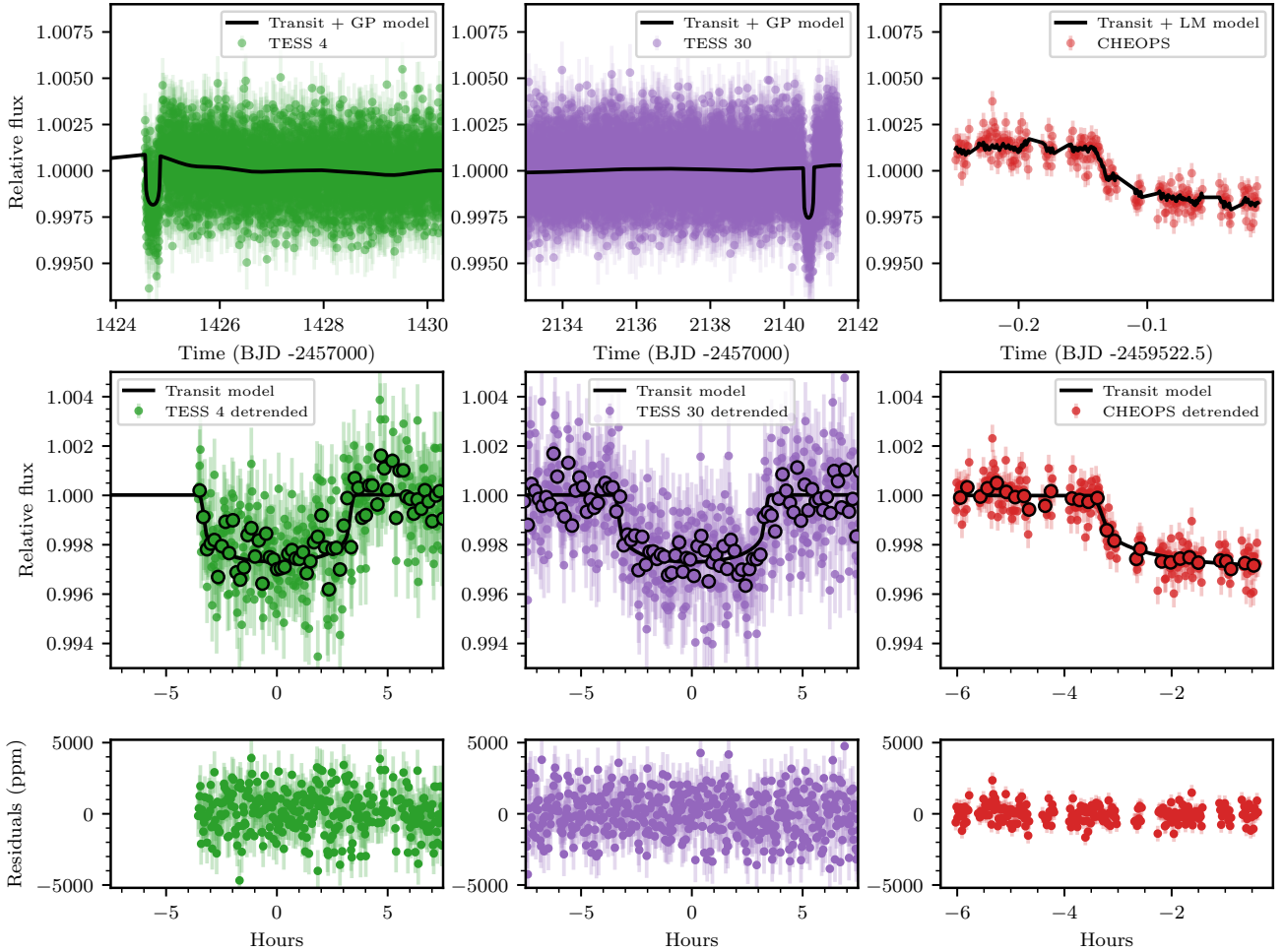


Fig. 6. Photometric observations of TOI-5678. Top row: Light curves from both TESS sectors (green and purple dots) and CHEOPS observation (red dots). The full median model is plotted as a black line. Middle row: detrended and phase-folded data from both TESS sectors (green and purple dots) and the CHEOPS observation (red dots). The phase-folded transit model is displayed in black. The dots outlined in black in all three panels show the ten-minute binned data. Bottom row: residuals in parts per million between the full model and the respective light curve.

To illustrate the amplitude of the signal that would be seen by a *James Webb* Space Telescope (JWST) observation, we computed synthetic transmission spectra of TOI-5678 b using the PYRAT BAY modeling framework (Cubillos & Blečić 2021). For simplicity, we assumed an atmosphere in thermochemical equilibrium at the planet’s equilibrium temperature and simulated two different metallicities: $70\times$ and $10\times$ solar. For reference, the C/H ratio for Neptune and Uranus (of similar mass to TOI-5678 b) is estimated to be $80 \pm 20\times$ solar (e.g., Atreya et al. 2020). Figure 8 shows the model spectra along with simulated observations from the JWST NIRSpec/G395H and NIRISS/SOSS instruments (Batalha et al. 2017). The spectra are generally dominated by H_2O bands, but a $3.5\ \mu\text{m}$ CH_4 feature and a $4.4\ \mu\text{m}$ CO_2 feature are also visible. The two metallicity cases show detectable variations in the molecular absorption features.

The planet is also suitable for obliquity measurement (Rossiter 1924; McLaughlin 1924). We calculated that TOI-5678 b produces a Rossiter-McLaughlin effect of $7\ \text{ms}^{-1}$ (Eq. (40) from Winn 2010), a value large enough to be measured with state-of-the-art high-resolution spectrographs, such as ESPRESSO (Pepe et al. 2021). Only a couple of gas giants with orbital periods longer than 40 days have an obliquity measurement, while no measurement has been done for Neptune-type planets at such long periods. On the one hand, Albrecht et al.

(2022) note that warm Jupiters and sub-Saturns with scaled semi-major axis (a/R_\star) larger than ten have relatively high obliquities. On the other hand, Rice et al. (2022) have found that tidally detached warm Jupiters appear more aligned than hot Jupiters; however, the authors also show that Saturn-type objects can have a wide range of obliquities. An obliquity measurement for TOI-5678 can help shed light on its formation and evolution mechanisms.

4.3. Formation and composition of TOI-5678 b

We applied a Bayesian inference scheme to model the internal structure of TOI-5678 b. A thorough description of the used method, which is based on Dorn et al. (2017), can be found in Leleu et al. (2021). In the following, we briefly summarize the most important aspects of the model: the assumed priors, the input parameters, and the forward model that was used to calculate the likelihood of a set of internal structure parameters.

For the priors, we assumed a distribution that is uniform on the simplex for the layer mass fractions of the iron core, silicate mantle, and the water layer, all with respect to the solid core of the planet (without the H/He atmosphere layer). We set an upper limit of 50% for the water mass fraction, following Thiabaud et al. (2014). For the gas mass fraction, a log-uniform distribution was assumed. It is important to note that the results of the

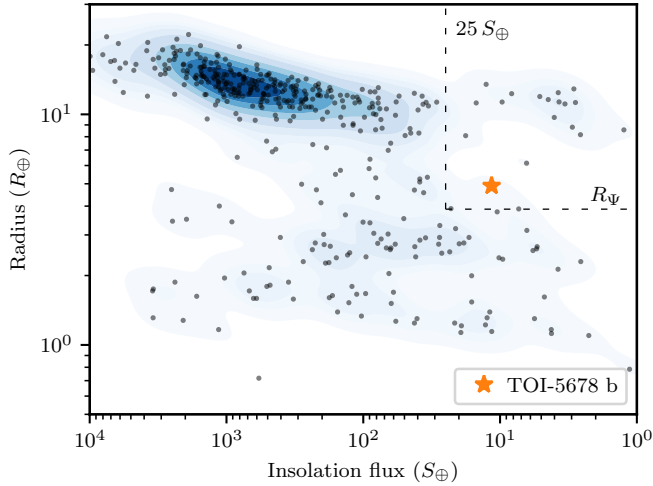


Fig. 7. Planetary radius as a function of stellar insolation for exoplanets with radius and mass uncertainties lower than 8 and 20%, respectively.

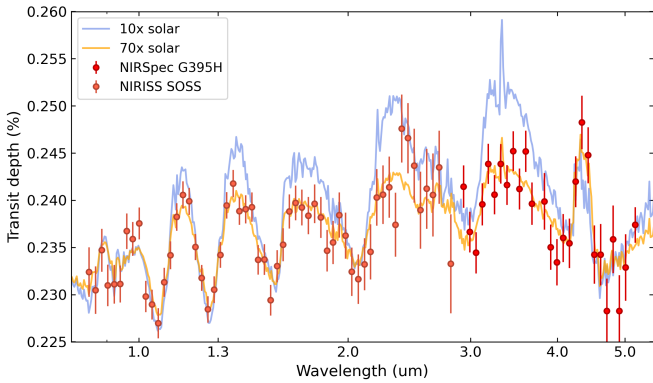


Fig. 8. Modeled transmission spectra of the target in the NIRSpect/G395H and NIRISS wavelength ranges for two possible metallicities, 10× (blue line) and 70× (orange line) solar. Simulated flux measurements of each instrument are displayed as red points for NIRSpect and as orange ones for NIRISS.

internal structure model depend to a certain extent on the chosen priors. The Bayesian inference model takes both planetary and stellar observables as input parameters: the mass, radius, age, effective temperature, and molecular abundances ([Si/H], [Mg/H], and [Fe/H]) of the star and the transit depth, relative mass, and period of the planet.

Finally, the forward model we selected assumes a spherically symmetric planet with four fully distinct layers (iron core, silicate mantle, water, and H/He atmosphere). It uses equations of state from [Hakim et al. \(2018\)](#), [Sotin et al. \(2007\)](#), [Haldemann et al. \(2020\)](#), and [Lopez & Fortney \(2014\)](#). We stress that in the current version of our model, the H/He atmosphere was modeled independently from the solid part of the planet, and we assumed a fixed temperature and pressure at the water-gas boundary, thereby neglecting the effects of the gas layer on the remaining layers of the planet. Moreover, we made the assumption that the Si/Mg/Fe ratios of the planet and the star are identical (see e.g., [Thiabaud et al. 2015](#)). We note that more recent results by [Adibekyan et al. \(2021\)](#) confirm that there is a correlation between the composition of a star and its planets, but the authors suggest a relationship that is not 1:1.

Figure 9 shows the results of the internal structure model. While the mass of the H/He layer of TOI-5678 b is reasonably

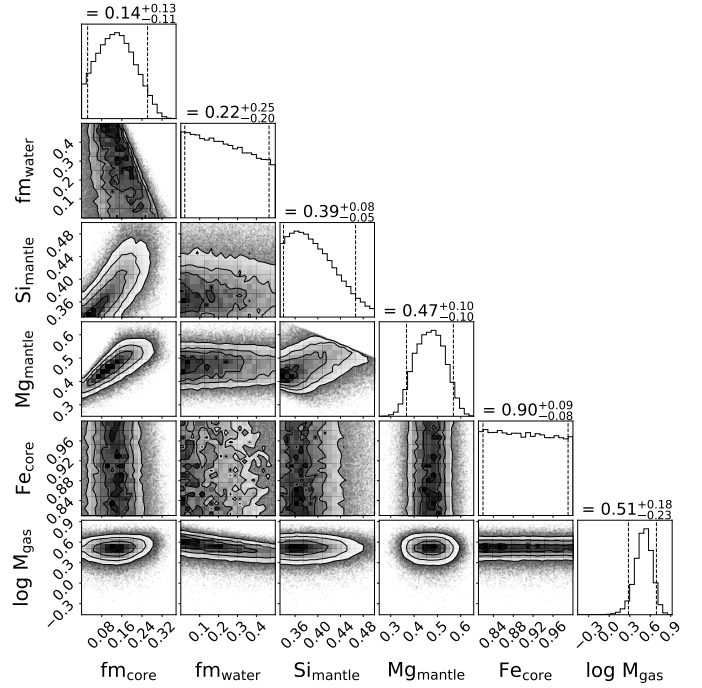


Fig. 9. Posterior distributions of the internal structure parameters of TOI-5678 b. The median and the five and 95 percentiles shown in the title of each column. The depicted internal structure parameters are: the layer mass fractions of the iron core and water layer with respect to the solid planet, the molar fractions of Si and Mg in the mantle and Fe in the core, and the logarithm of the gas mass in Earth masses.

well constrained and quite large, with $3.2^{+1.7}_{-1.3} M_{\oplus}$, the posterior of the water mass fraction is almost completely unconstrained. The molar fraction of iron in the core (Fe_{core}) is also unconstrained and only varies between the bounds allowed by its prior. Furthermore, the posterior distribution of the radius of the gas layer has a median of $2.53^{+0.32}_{-0.34} R_{\oplus}$. By combining the planet mass with the inferred mass of H-He, we predicted a minimum mass of $11.1 M_{\oplus}$ of heavy elements for TOI-5678 b. A planet with such a large content of heavy elements likely accreted its core beyond the ice line (e.g., [Venturini et al. 2020a,b](#)).

We compared TOI-5678 b to synthetic planets with similar parameters produced with the New Generation Planetary Population Synthesis ([Mordasini et al. 2009](#)), the latest version of the Bern model ([Emsenhuber et al. 2021a,b](#)) available on DACE¹¹. We chose the NG76 simulation where 100 embryos are used. We found that synthetic planets with a radius, mass, and semi-major axis close to TOI-5678b form at a couple of astronomical units from their host star. After a first initial growth up to about $10 M_{\oplus}$, the planets migrate inwards while steadily accreting mass but without reaching a mass high enough to trigger rapid gas accretion. These planets are part of the system architecture called migrated sub-Neptunes (Class II), as described in [Emsenhuber et al. \(2023\)](#). We note that some planets can also reach about $20 M_{\oplus}$ by accreting a significant amount of their mass through collisions. These planets forming through giant impacts originate from inside the ice line, and their final planetary radius is usually below $3 R_{\oplus}$. In contrast, planets originating from outside the ice line have a larger radius, and they contain a significant fraction of gas, similar to what we estimated for TOI-5678 b. The knowledge of both mass and radius of TOI-5678 b allows us to favor a formation and migration scenario starting outside

¹¹ dace.unige.ch/populationAnalysis

of the ice line. This is also supported by other formation models, which find that only water-rich planets account for planets with masses larger than $10 M_{\oplus}$ and radii larger than $3 R_{\oplus}$ (Venturini et al. 2020a, Figs. D1 and D2). This support reinforces the likelihood that TOI-5678 b formed beyond the ice line and migrated inwards later on. Finally, the nearly circular orbit of TOI-5678 b and long circularization timescale suggest that the hypothesis of a planet-disk migration is favored over a high eccentricity migration scenario. This migration hypothesis can be tested via the measurement of the spin-orbit alignment of the system.

5. Conclusions

This paper reports the discovery TOI-5678 b, a transiting long-period Neptune-mass planet. Its host is a G7V-type star of solar metallicity with an age of 8.5 ± 3.0 Gyr. The planet itself is on an almost circular orbit and has an orbital period of 47.73 days. Its planetary mass is equal to $20 \pm 4 M_{\oplus}$, and its planetary radius is equal to $4.91 \pm 0.08 R_{\oplus}$. We used the space-based photometric satellites TESS and CHEOPS to identify and confirm the orbital period of TOI-5678 b. We combined the photometric data with CORALIE and HARPS radial velocities to characterize the system and measure the mass and eccentricity of the transiting companion. We modeled the interior structure of TOI-5678 b and constrained the mass of its H/He layer to $3.2^{+1.7}_{-1.3} M_{\oplus}$, assuming the four-layer model presented in Sect. 4.3. We show that TOI-5678 b likely formed beyond the ice line and then migrated inwards to its current location. The long orbital period of TOI-5678 b prevents it from undergoing strong dynamical interactions with the host star. Additional observations, such as Rossiter-McLaughlin measurements, would further improve our knowledge of the system. Such long-period intermediate-mass planets as TOI-5678 b provide the opportunity to bridge exoplanet and Solar System science, providing key information on the Uranus- and Neptune-like planets.

Acknowledgements. This work has been carried out within the framework of the National Centre of Competence in Research PlanetS supported by the Swiss National Science Foundation under grants 51NF40_182901 and 51NF40_205606. The authors acknowledge the financial support of the SNSF. A.T. acknowledges support from an STFC PhD studentship. M.L. acknowledges support of the Swiss National Science Foundation under grant number PCEFP2194576. P.M. acknowledges support from STFC research grant number ST/M001040/1. J.E., Y.A., and M.J.H. acknowledge the support of the Swiss National Fund under grant 200020_172746. A.Br. was supported by the SNSA. M.F. and C.M.P. gratefully acknowledge the support of the Swedish National Space Agency (DNR 65/19, 174/18, 177/19). D.G. and L.M.S. gratefully acknowledge financial support from the CRT foundation under Grant No. 2018.2323 “Gaseous or rocky? Unveiling the nature of small worlds”. C.M. acknowledges the support from the SNSF under grant 200021_204847 “PlanetsInTime”. S.G.S. acknowledges support from FCT through FCT contract nr. CEECIND/00826/2018 and POPH/FSE (EC). A.C.C. and T.W. acknowledge support from STFC consolidated grant numbers ST/R000824/1 and ST/V000861/1, and UKSA grant number ST/R003203/1. We acknowledge support from the Spanish Ministry of Science and Innovation and the European Regional Development Fund through grants ESP2016-80435-C2-1-R, ESP2016-80435-C2-2-R, PGC2018-098153-B-C33, PGC2018-098153-B-C31, ESP2017-87676-C5-1-R, MDM-2017-0737 Unidad de Excelencia Maria de Maeztu-Centro de Astrobiología (INTA-CSIC), as well as the support of the Generalitat de Catalunya/CERCA programme. The MOC activities have been supported by the ESA contract No. 4000124370. S.C.C.B. acknowledges support from FCT through FCT contracts nr. IF/01312/2014/CP1215/CT0004. X.B., S.C., D.G., M.F. and J.L. acknowledge their role as ESA-appointed CHEOPS science team members. This project was supported by the CNES. The Belgian participation to CHEOPS has been supported by the Belgian Federal Science Policy Office (BELSPO) in the framework of the PRODEX Program, and by the University of Liège through an ARC grant for Concerted Research Actions financed by the Wallonia-Brussels Federation; L.D. is an F.R.S.-FNRS Postdoctoral Researcher. This work was supported by FCT – Fundação para a Ciência e a Tecnologia through national funds and by FEDER through COMPETE2020

– Programa Operacional Competitividade e Internacionalização by these grants: UID/FIS/04434/2019, UIDB/04434/2020, UIDP/04434/2020, PTDC/FIS-AST/32113/2017 & POCI-01-0145-FEDER-032113, PTDC/FIS-AST/28953/2017 & POCI-01-0145-FEDER-028953, PTDC/FIS-AST/28987/2017 & POCI-01-0145-FEDER-028987, O.D.S.D. is supported in the form of work contract (DL 57/2016/CP1364/CT0004) funded by national funds through FCT. This project has received funding from the European Research Council (ERC) under the European Union’s Horizon 2020 research and innovation programme (grant agreement SCORE No 851555). J.H. supported by the Swiss National Science Foundation (SNSF) through the Ambizione grant #PZ00P2_180098. P.E.C. is funded by the Austrian Science Fund (FWF) Erwin Schrodinger Fellowship, program J4595-N. B.-O.D. acknowledges support from the Swiss State Secretariat for Education, Research and Innovation (SERI) under contract number MB22.00046 and from the Swiss National Science Foundation (PP00P2-190080). This project has received funding from the European Research Council (ERC) under the European Union’s Horizon 2020 research and innovation programme (project FOUR ACES; grant agreement No 724427). It has also been carried out in the frame of the National Centre for Competence in Research PlanetS supported by the Swiss National Science Foundation (SNSF). D.E. acknowledges financial support from the Swiss National Science Foundation for project 200021_200726. M.G. and V.V.G. are F.R.S.-FNRS Senior Research Associates. S.H. gratefully acknowledges CNES funding through the grant 837319. This work was granted access to the HPC resources of MesoPSL financed by the Region Ile de France and the project Equip@Meso (reference ANR-10-EQPX-29-01) of the programme Investissements d’Avenir supervised by the Agence Nationale pour la Recherche. L.Bo., G.Br., V.Na., I.Pa., G.Pi., R.Ra., G.Sc., V.Si., and T.Zi. acknowledge support from CHEOPS ASI-INAF agreement n. 2019-29-HH.0. This work was also partially supported by a grant from the Simons Foundation (PI: Queloz, grant number 327127). I.R.I. acknowledges support from the Spanish Ministry of Science and Innovation and the European Regional Development Fund through grant PGC2018-098153-B-C33, as well as the support of the Generalitat de Catalunya/CERCA programme. Gy.M.Sz. acknowledges the support of the Hungarian National Research, Development and Innovation Office (NKFIH) grant K-125015, a PRODEX Experiment Agreement No. 4000137122, the Lendület LP2018-7/2021 grant of the Hungarian Academy of Science and the support of the city of Szombathely. N.A.W. acknowledges UKSA grant ST/R004838/1. K.G.I. is the ESA CHEOPS Project Scientist and is responsible for the ESA CHEOPS Guest Observers Programme. She does not participate in, or contribute to, the definition of the Guaranteed Time Programme of the CHEOPS mission through which observations described in this paper have been taken, nor to any aspect of target selection for the programme. The authors acknowledge the use of public TESS data from pipelines at the TESS Science Office and at the TESS Science Processing Operations Centre.

References

- Adams, F. C., & Laughlin, G. 2006, *ApJ*, **649**, 1004
- Adibekyan, V. Z., Sousa, S. G., Santos, N. C., et al. 2012, *A&A*, **545**, A32
- Adibekyan, V., Figuera, P., Santos, N. C., et al. 2015, *A&A*, **583**, A94
- Adibekyan, V., Dorn, C., Sousa, S. G., et al. 2021, *Science*, **374**, 330
- Albrecht, S. H., Dawson, R. I., & Winn, J. N. 2022, *PASP*, **134**, 1038
- Aller, A., Lillo-Box, J., Jones, D., Miranda, L. F., & Barceló Forteza, S. 2020, *A&A*, **635**, A128
- Atreya, S. K., Hofstadter, M. H., In, J. H., et al. 2020, *Space Sci. Rev.*, **216**, 18
- Banfield, D., & Murray, N. 1992, *Icarus*, **99**, 390
- Barros, S. C. C., Akisanmi, B., Boué, G., et al. 2022, *A&A*, **657**, A52
- Bashi, D., Helled, R., Zucker, S., & Mordasini, C. 2017, *A&A*, **604**, A83
- Batalha, N. E., Mandell, A., Pontoppidan, K., et al. 2017, *PASP*, **129**, 064501
- Benz, W., Broeg, C., Fortier, A., et al. 2021, *Exp. Astron.*, **51**, 109
- Blackwell, D. E., & Shallis, M. J. 1977, *MNRAS*, **180**, 177
- Bonfanti, A., Ortolani, S., Piovato, G., & Nascimbeni, V. 2015, *A&A*, **575**, A18
- Bonfanti, A., Ortolani, S., & Nascimbeni, V. 2016, *A&A*, **585**, A5
- Bonfanti, A., Delrez, L., Hooton, M. J., et al. 2021, *A&A*, **646**, A157
- Bonomo, A. S., Desidera, S., Benatti, S., et al. 2016, *Celest. Mech. Dyn. Astron.*, **126**, 145
- Borucki, W. J., Koch, D., Basri, G., et al. 2010, *Science*, **327**, 977
- Bruntt, H., Bedding, T. R., Quirion, P. O., et al. 2010, *MNRAS*, **405**, 1907
- Castelli, F., & Kurucz, R. L. 2003, *A&A*, **210**, A20
- Cubillos, P. E., & Blecic, J. 2021, *MNRAS*, **505**, 2675
- Dalba, P. A., Gupta, A. F., Rodriguez, J. E., et al. 2020, *AJ*, **159**, 241
- Dalba, P. A., Kane, S. R., Isaacson, H., et al. 2021, *AJ*, **161**, 103
- Dalba, P. A., Kane, S. R., Dragomir, D., et al. 2022, *AJ*, **163**, 61
- Deline, A., Queloz, D., Chazelas, B., et al. 2020, *A&A*, **635**, A22
- Delrez, L., Ehrenreich, D., Alibert, Y., et al. 2021, *Nat. Astron.*, **5**, 775
- Dorn, C., Venturini, J., Khan, A., et al. 2017, *A&A*, **597**, A37
- Doyle, A. P., Davies, G. R., Smalley, B., Chaplin, W. J., & Elsworth, Y. 2014, *MNRAS*, **444**, 3592

- Dransfield, G., Triaud, A. H. M. J., Guillot, T., et al. 2022, *MNRAS*, **515**, 1328
- Dubber, S. C., Mortier, A., Rice, K., et al. 2019, *MNRAS*, **490**, 5103
- Emsenhuber, A., Mordasini, C., Burn, R., et al. 2021a, *A&A*, **656**, A69
- Emsenhuber, A., Mordasini, C., Burn, R., et al. 2021b, *A&A*, **656**, A70
- Emsenhuber, A., Mordasini, C., & Burn, R. 2023, *Planetary Population Synthesis and the Emergence of Four Classes of Planetary System Architectures* (Berlin: Springer)
- Espinoza, N., & Jordán, A. 2015, *MNRAS*, **450**, 1879
- Espinoza, N., Kossakowski, D., & Brahm, R. 2019, *MNRAS*, **490**, 2262
- Faria, J. P., Santos, N. C., Figueira, P., & Brewer, B. J. 2018, *J. Open Source Softw.*, **3**, 487
- Feroz, F., Balan, S. T., & Hobson, M. P. 2011, *MNRAS*, **415**, 3462
- Foreman-Mackey, D., Morton, T. D., Hogg, D. W., Agol, E., & Schölkopf, B. 2016, *AJ*, **152**, 206
- Fridlund, C. V. M. 2008, *Phys. Scrip. Vol. T*, **130**, 014009
- Fridlund, M., Livingston, J., Gandolfi, D., et al. 2020, *MNRAS*, **498**, 4503
- Fulton, B. J., Petigura, E. A., Blunt, S., & Sinukoff, E. 2018, *PASP*, **130**, 044504
- Fulton, B. J., Rosenthal, L. J., Hirsch, L. A., et al. 2021, *ApJS*, **255**, 14
- Gaia Collaboration (Brown, A. G. A., et al.) 2021, *A&A*, **649**, A1
- Garai, Z., Osborn, P., Gandolfi, D., et al. 2023, *A&A*, **674**, A44
- Gill, S., Bayliss, D., Cooke, B. F., et al. 2020a, *MNRAS*, **491**, 1548
- Gill, S., Wheatley, P. J., Cooke, B. F., et al. 2020b, *ApJ*, **898**, L11
- Gray, D. F. 2008, *The Observation and Analysis of Stellar Photospheres* (Cambridge: Cambridge University Press)
- Gustafsson, B., Edvardsson, B., Eriksson, K., et al. 2008, *A&A*, **486**, 951
- Hakim, K., Rivoldini, A., Van Hoolst, T., et al. 2018, *Icarus*, **313**, 61
- Haldemann, J., Alibert, Y., Mordasini, C., & Benz, W. 2020, *A&A*, **643**, A105
- Helled, R., & Bodenheimer, P. 2014, *ApJ*, **789**, 69
- Hobson, M. J., Brahm, R., Jordán, A., et al. 2021, *AJ*, **161**, 235
- Høg, E., Fabricius, C., Makarov, V. V., et al. 2000, *A&A*, **355**, L27
- Hoyer, S., Guterman, P., Demangeon, O., et al. 2020, *A&A*, **635**, A24
- Husser, T.-O., Wende-von Berg, S., Dreizler, S., et al. 2013, *A&A*, **553**, A6
- Jackson, B., Greenberg, R., & Barnes, R. 2008, *ApJ*, **678**, 1396
- Jenkins, J. M., Twicken, J. D., McCauliff, S., et al. 2016, *SpIE*, **9913**, 99133E
- Kempton, E. M. R., Bean, J. L., Louie, D. R., et al. 2018, *PASP*, **130**, 114401
- Kipping, D. 2018, *RNAAS*, **2**, 223
- Kipping, D. M. 2013a, *MNRAS*, **435**, 2152
- Kipping, D. M. 2013b, *MNRAS*, **434**, L51
- König, P. C., Damasso, M., Hébrard, G., et al. 2022, *A&A*, **666**, A183
- Kovács, G., Zucker, S., & Mazeh, T. 2002, *A&A*, **391**, 369
- Kreidberg, L. 2015, *PASP*, **127**, 1161
- Kurucz, R. L. 1979, *ApJS*, **40**, 1
- Kurucz, R. L. 1993, *SYNTHES Spectrum Synthesis Programs and Line Data* (Cambridge, Mass.: Smithsonian Astrophysical Observatory)
- Lacedelli, G., Wilson, T. G., Malavolta, L., et al. 2022, *MNRAS*, **511**, 4551
- Lainey, V., Arlot, J.-E., Karatekin, Ö., & van Hoolst, T. 2009, *Nature*, **459**, 957
- Leleu, A., Alibert, Y., Hara, N. C., et al. 2021, *A&A*, **649**, A26
- Lendl, M., Csizmadia, S., Deline, A., et al. 2020, *A&A*, **643**, A94
- Lindgren, L., Bastian, U., Biermann, M., et al. 2021, *A&A*, **649**, A4
- Lopez, E. D., & Fortney, J. J. 2014, *ApJ*, **792**, 1
- Lovis, C., & Pepe, F. 2007, *A&A*, **468**, 1115
- Mancini, L., Lillo-Box, J., Southworth, J., et al. 2016, *A&A*, **590**, A112
- Marigo, P., Girardi, L., Bressan, A., et al. 2017, *ApJ*, **835**, 77
- Mayor, M., Pepe, F., Queloz, D., et al. 2003, *The Messenger*, **114**, 20
- Mayor, M., Marmier, M., Lovis, C., et al. 2011, ArXiv e-prints [arXiv:1109.2497]
- McLaughlin, D. B. 1924, *ApJ*, **60**, 22
- Miller, N., & Fortney, J. J. 2011, *ApJ*, **736**, L29
- Montalto, M., Borsato, L., Granata, V., et al. 2020, *MNRAS*, **498**, 1726
- Mordasini, C., Alibert, Y., & Benz, W. 2009, *A&A*, **501**, 1139
- Osborn, H. P. 2022, *Astrophysics Source Code Library* [record [ascl:2204.020](#)]
- Osborn, H. P., Bonfanti, A., Gandolfi, D., et al. 2022, *A&A*, **664**, A156
- Osborn, H. P., Nowak, G., Hébrard, G., et al. 2023, *MNRAS*, **523**, 3069
- Otegi, J. F., Bouchy, F., & Helled, R. 2020, *A&A*, **634**, A43
- Pepe, F., Mayor, M., Rupprecht, G., et al. 2002, *The Messenger*, **110**, 9
- Pepe, F., Cristiani, S., Rebolo, R., et al. 2021, *A&A*, **645**, A96
- Petigura, E. A., Marcy, G. W., Winn, J. N., et al. 2018, *AJ*, **155**, 89
- Piskunov, N., & Valenti, J. A. 2017, *A&A*, **597**, A16
- Piskunov, N. E., Kupka, F., Ryabchikova, T. A., Weiss, W. W., & Jeffery, C. S. 1995, *A&AS*, **112**, 525
- Queloz, D., Mayor, M., Udry, S., et al. 2001, *The Messenger*, **105**, 1
- Rice, M., Wang, S., Wang, X.-Y., et al. 2022, *AJ*, **164**, 104
- Ricker, G. R., Winn, J. N., Vanderspek, R., et al. 2015, *J. Astron. Teles. Instrum. Syst.*, **1**, 014003
- Rossiter, R. A. 1924, *ApJ*, **60**, 15
- Salmon, S. J. A. J., Van Grootel, V., Buldgen, G., Dupret, M.-A., & Eggenberger, P. 2021, *A&A*, **646**, A7
- Santos, N. C., Sousa, S. G., Mortier, A., et al. 2013, *A&A*, **556**, A150
- Schanche, N., Hébrard, G., Collier Cameron, A., et al. 2020, *MNRAS*, **499**, 428
- Scuflaire, R., Théado, S., Montalbán, J., et al. 2008, *Astrophys. Space Sci.*, **316**, 83
- Skrutskie, M. F., Cutri, R. M., Stiening, R., et al. 2006, *AJ*, **131**, 1163
- Snedden, C. A. 1973, PhD thesis, University of Texas, USA
- Sotin, C., Grasset, O., & Mocquet, A. 2007, *Icarus*, **191**, 337
- Sousa, S. G. 2014, *ARES + MOOG: A Practical Overview of an Equivalent Width (EW) Method to Derive Stellar Parameters* (Berlin: Springer), 297
- Sousa, S. G., Santos, N. C., Israelian, G., Mayor, M., & Monteiro, M. J. P. F. G. 2007, *A&A*, **469**, 783
- Sousa, S. G., Santos, N. C., Mayor, M., et al. 2008, *A&A*, **487**, 373
- Sousa, S. G., Santos, N. C., Adibekyan, V., Delgado-Mena, E., & Israelian, G. 2015, *A&A*, **577**, A67
- Sousa, S. G., Adibekyan, V., Delgado-Mena, E., et al. 2021, *A&A*, **656**, A53
- Speagle, J. S. 2019, ArXiv e-prints [arXiv:1909.12313]
- Stassun, K. G., Oelkers, R. J., Paegert, M., et al. 2019, *AJ*, **158**, 138
- Szabó, G. M., Gandolfi, D., Brandeker, A., et al. 2021, *A&A*, **654**, A159
- Thiabaud, A., Marboeuf, U., Alibert, Y., et al. 2014, *A&A*, **562**, A27
- Thiabaud, A., Marboeuf, U., Alibert, Y., Laya, I., & Mezger, K. 2015, *A&A*, **580**, A30
- Thorngren, D. P., Fortney, J. J., Murray-Clay, R. A., & Lopez, E. D. 2016, *ApJ*, **831**, 64
- Tuson, A., & the CHEOPS Consortium 2022, 16th Europlanet Science Congress 2022, 16, EPSC2022-499
- Tuson, A., Queloz, D., Osborn, H. P., et al. 2023, *MNRAS*, **523**, 3090
- Uehara, S., Kawahara, H., Masuda, K., Yamada, S., & Aizawa, M. 2016, *ApJ*, **822**, 2
- Ulmer-Moll, S., Lendl, M., Gill, S., et al. 2022, *A&A*, **666**, A46
- Valenti, J. A., & Piskunov, N. 1996, *Astron. Astrophys. Suppl. Ser.*, **118**, 595
- Valletta, C., & Helled, R. 2022, *ApJ*, **931**, 21
- Venturini, J., Guilera, O. M., Haldemann, J., Ronco, M. P., & Mordasini, C. 2020a, *A&A*, **643**, L1
- Venturini, J., Guilera, O. M., Ronco, M. P., & Mordasini, C. 2020b, *A&A*, **644**, A174
- Wang, J., Fischer, D. A., Barclay, T., et al. 2015, *ApJ*, **815**, 127
- Winn, J. N. 2010, *Exoplanet Transits and Occultations* (Tucson: University of Arizona Press)
- Wright, E. L., Eisenhardt, P. R. M., Mainzer, A. K., et al. 2010, *AJ*, **140**, 1868
- Zechmeister, M., & Kürster, M. 2009, *A&A*, **496**, 577

¹ Observatoire Astronomique de l'Université de Genève, Chemin Pegasi 51, 1290 Versoix, Switzerland
e-mail: solene.ulmer-moll@astro.up.pt

² Physikalisches Institut, University of Bern, Gesellschaftsstrasse 6, 3012 Bern, Switzerland

³ Department of Physics and Kavli Institute for Astrophysics and Space Research, Massachusetts Institute of Technology, Cambridge, MA 02139, USA

⁴ Astrophysics Group, Cavendish Laboratory, University of Cambridge, J.J. Thomson Avenue, Cambridge CB3 0HE, UK

⁵ Astrophysics Group, Keele University, Staffordshire, ST5 5BG, UK

⁶ Department of Astronomy, Stockholm University, AlbaNova University Center, 10691 Stockholm, Sweden

⁷ Instituto de Astrofísica e Ciências do Espaço, Universidade do Porto, CAUP, Rua das Estrelas, 4150-762 Porto, Portugal

⁸ Space Research Institute, Austrian Academy of Sciences, Schmiedlstrasse 6, 8042 Graz, Austria

⁹ Leiden Observatory, University of Leiden, PO Box 9513, 2300 RA Leiden, The Netherlands

¹⁰ Department of Space, Earth and Environment, Chalmers University of Technology, Onsala Space Observatory, 439 92 Onsala, Sweden

¹¹ Dipartimento di Fisica, Università degli Studi di Torino, via Pietro Giuria 1, 10125 Torino, Italy

- ¹² Centre for Exoplanet Science, SUPA School of Physics and Astronomy, University of St Andrews, North Haugh, St Andrews KY16 9SS, UK
- ¹³ ESTEC, European Space Agency, 2201 AZ Noordwijk, The Netherlands
- ¹⁴ INAF – Osservatorio Astrofisico di Catania, Via S. Sofia 78, 95123 Catania, Italy
- ¹⁵ German Aerospace Center (DLR), Institute of Optical Sensor Systems Rutherfordstraße 2, 12489 Berlin, Germany
- ¹⁶ Instituto de Astrofísica de Canarias, 38200 La Laguna, Tenerife, Spain
- ¹⁷ Departamento de Astrofísica, Universidad de La Laguna, 38206 La Laguna, Tenerife, Spain
- ¹⁸ Institut de Ciències de l’Espai (ICE, CSIC), Campus UAB, Can Magrans s/n, 08193 Bellaterra, Spain
- ¹⁹ Institut d’Estudis Espacials de Catalunya (IEEC), 08034 Barcelona, Spain
- ²⁰ Depto. de Astrofísica, Centro de Astrobiología (CSIC-INTA), ESAC campus, 28692 Villanueva de la Cañada (Madrid), Spain
- ²¹ Departamento de Física e Astronomia, Faculdade de Ciências, Universidade do Porto, Rua do Campo Alegre, 4169-007 Porto, Portugal
- ²² Center for Space and Habitability, University of Bern, Gesellschaftsstrasse 6, 3012 Bern, Switzerland
- ²³ Université Grenoble Alpes, CNRS, IPAG, 38000 Grenoble, France
- ²⁴ INAF, Osservatorio Astronomico di Padova, Vicolo dell’Osservatorio 5, 35122 Padova, Italy
- ²⁵ Admatis, 5. Kándó Kálmán Street, 3534 Miskolc, Hungary
- ²⁶ Institute of Planetary Research, German Aerospace Center (DLR), Rutherfordstrasse 2, 12489 Berlin, Germany
- ²⁷ Université de Paris, Institut de physique du globe de Paris, CNRS, 75005 Paris, France
- ²⁸ INAF – Osservatorio Astrofisico di Torino, Strada Osservatorio, 20 10025 Pino Torinese (TO), Italy
- ²⁹ Centre for Mathematical Sciences, Lund University, Box 118, 221 00 Lund, Sweden
- ³⁰ Aix-Marseille Univ, CNRS, CNES, LAM, 38 rue Frédéric Joliot-Curie, 13388 Marseille, France
- ³¹ Astrobiology Research Unit, Université de Liège, Allée du 6 Août 19C, 4000 Liège, Belgium
- ³² Space sciences, Technologies and Astrophysics Research (STAR) Institute, Université de Liège, Allée du 6 Août 19C, 4000 Liège, Belgium
- ³³ Centre Vie dans l’Univers, Faculté des sciences, Université de Genève, Quai Ernest-Ansermet 30, 1211 Genève 4, Switzerland
- ³⁴ Center for Computational Astrophysics, Flatiron Institute, New York, NY 10010, USA
- ³⁵ University of Vienna, Department of Astrophysics, Türkenschanzstrasse 17, 1180 Vienna, Austria
- ³⁶ Institute for Computational Science, University of Zurich, Winterthurerstr. 190, 8057 Zurich, Switzerland
- ³⁷ Science and Operations Department – Science Division (SCI-SC), Directorate of Science, European Space Agency (ESA), European Space Research and Technology Centre (ESTEC), Keplerlaan 1, 2201 AZ Noordwijk, The Netherlands
- ³⁸ Konkoly Observatory, Research Centre for Astronomy and Earth Sciences, 1121 Budapest, Konkoly Thege Miklós út 15-17, Hungary
- ³⁹ ELTE Eötvös Loránd University, Institute of Physics, Pázmány Péter sétány 1/A, 1117 Budapest, Hungary
- ⁴⁰ IMCCE, UMR8028 CNRS, Observatoire de Paris, PSL Univ., Sorbonne Univ., 77 av. Denfert-Rochereau, 75014 Paris, France
- ⁴¹ Institut d’astrophysique de Paris, UMR7095 CNRS, Université Pierre & Marie Curie, 98bis blvd. Arago, 75014 Paris, France
- ⁴² Department of Astrophysics, University of Vienna, Tuerkenschanzstrasse 17, 1180 Vienna, Austria
- ⁴³ Institute of Optical Sensor Systems, German Aerospace Center (DLR), Rutherfordstrasse 2, 12489 Berlin, Germany
- ⁴⁴ Dipartimento di Fisica e Astronomia “Galileo Galilei”, Università degli Studi di Padova, Vicolo dell’Osservatorio 3, 35122 Padova, Italy
- ⁴⁵ Department of Physics, University of Warwick, Gibbet Hill Road, Coventry CV4 7AL, UK
- ⁴⁶ ETH Zurich, Department of Physics, Wolfgang-Pauli-Strasse 2, 8093 Zurich, Switzerland
- ⁴⁷ Cavendish Laboratory, JJ Thomson Avenue, Cambridge CB3 0HE, UK
- ⁴⁸ Zentrum für Astronomie und Astrophysik, Technische Universität Berlin, Hardenbergstr. 36, 10623 Berlin, Germany
- ⁴⁹ ELTE Eötvös Loránd University, Gothard Astrophysical Observatory, 9700 Szombathely, Szent Imre h. u. 112, Hungary
- ⁵⁰ MTA-ELTE Exoplanet Research Group, 9700 Szombathely, Szent Imre h. u. 112, Hungary
- ⁵¹ Institute of Astronomy, University of Cambridge, Madingley Road, Cambridge, CB3 0HA, UK

Appendix A: Radial velocity modeling priors

Table A.1. Priors for the radial velocity fit.

Parameters	Distribution	Value
Number of planets	Uniform	(0, 1)
Orbital period (days)	LogUniform	(1, 161)
Semi-amplitude (ms^{-1})	LogUniform	(1, 136)
Eccentricity	Kumaraswamy	(0.867, 3.03)
Mean anomaly	Uniform	$(-\pi, \pi)$
Argument of periastron	Uniform	(0, 2π)
Jitter (ms^{-1})	LogUniform	(1, 200)

Appendix B: Joint modeling priors

Table B.1. Priors for the joint modeling of photometric and radial velocity data.

Parameters	Distribution	TOI-5678 b
Orbital period (days)	Uniform	(40, 60)
Time of transit T0 (days)	Uniform	(2458485.9, 2458486.3)
Radius ratio	Uniform	(0, 1)
Impact parameter	Uniform	(0, 1)
Stellar density	Normal	(685.24, 79.18)
TESS limb darkening q1	Normal	(0.274, 0.027)
TESS limb darkening q2	Normal	(0.275, 0.029)
CHEOPS limb darkening q1	Uniform	(0.47, 0.05)
CHEOPS limb darkening q2	Uniform	(0.363, 0.015)
Eccentricity	Kumaraswamy / fixed	(0.867, 3.03)
Argument of periastron	Uniform	(0, 2π)
TESS offsets	Normal	(0, 0.01)
TESS jitters (ppm)	LogUniform	(0.1, 1000)
CHEOPS offsets	Normal	(0, 0.01)
CHEOPS jitters (ppm)	LogUniform	(0.1, 1000)
GP amplitude TESS (relative flux)	LogUniform	(1e-06, 100.0)
GP time-scale TESS (days)	LogUniform	(0.001, 100.0)
GP amplitude TESS 2 (relative flux)	LogUniform	(1e-06, 100.0)
GP time-scale TESS 2 (days)	LogUniform	(0.001, 100.0)
Background CHEOPS (relative flux)	LogUniform	(-1, 1)
$\cos(2\theta)$ CHEOPS (days)	Uniform	(-1, 1)
$\cos(3\theta)$ CHEOPS (days)	Uniform	(-1, 1)
X coordinate CHEOPS	LogUniform	(-1, 1)
Y coordinate CHEOPS	Uniform	(-1, 1)
Semi-amplitude (kms^{-1})	Uniform	(0, 100)
Spectrograph offsets (kms^{-1})	Uniform	(-100, 100)
Spectrograph jitters (kms^{-1})	LogUniform	(0.001, 0.2)

Notes. The normal distribution is defined by its mean and variance. The uniform and log-uniform distributions were defined with the lower and upper bounds of the distribution. The priors on the radial velocity offsets and jitters are identical for CORALIE and HARPS.

Appendix C: Joint modeling posterior distribution

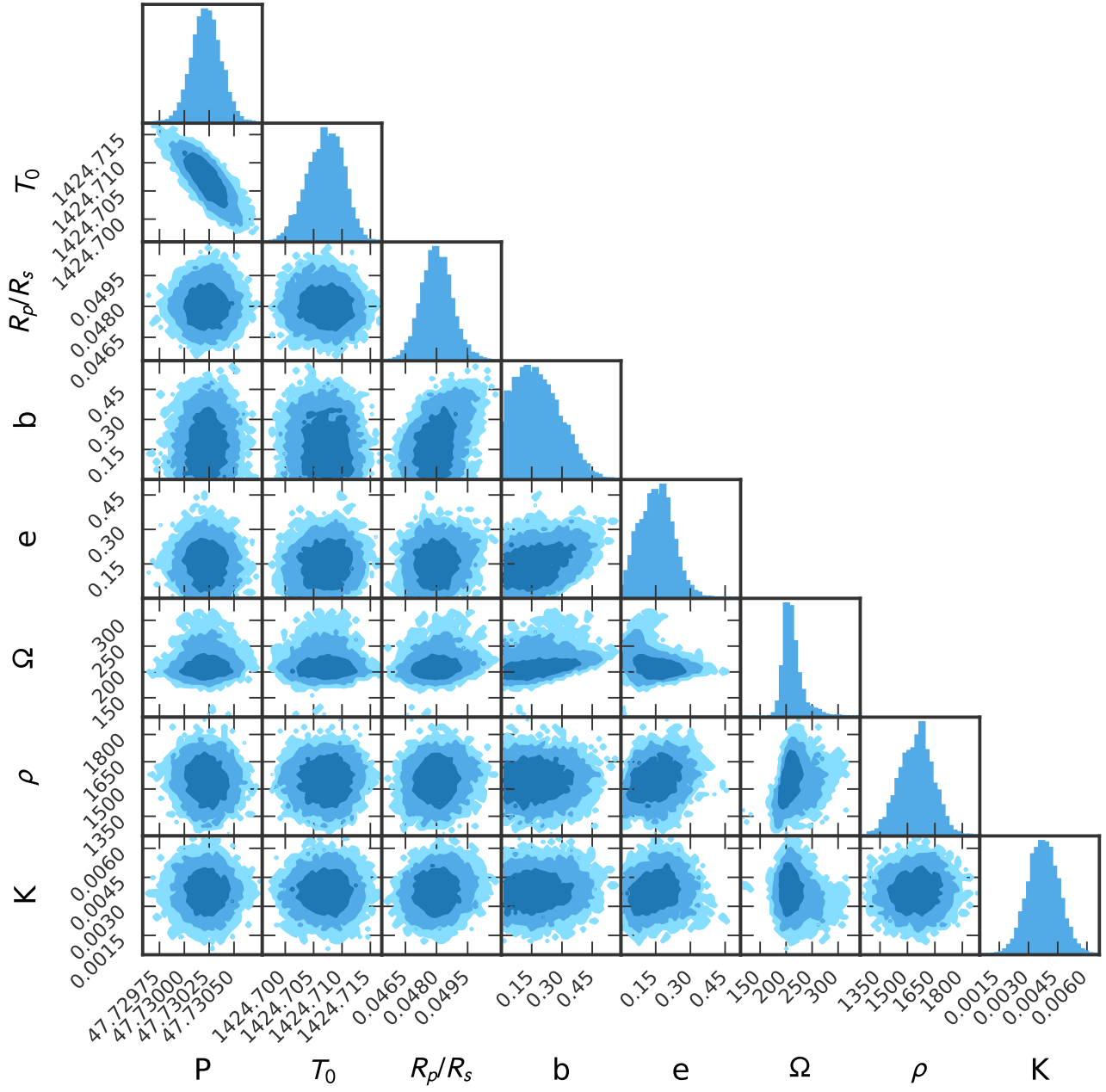


Fig. C.1. Posterior distributions of fitted parameters for TOI-5678 b along with the stellar density (ρ) and radial velocity semi-amplitude (K).